SusMat

WILEY

SusMat

RESEARCH ARTICLE OPEN ACCESS

Effects of B-Site Nb Substitution on ORR Activity in Perovskite Cathode Materials for Solid Oxide Fuel Cells

Qiuchun Lu[1] | Yufei Zhang[1] | Yongkang Tan[2] | Tianchuan Qian[3] | Jiaxin Yan[3] | Feng Jiang[1] | Adit Gupta[1] | Stefano Botticini[4] | Federica Rigoni[4] | Elisabetta Comini[4] | Daniel H. C. Chua[3] | Pooi See Lee[1]

[1]School of Materials Science and Engineering, Nanyang Technological University, Singapore | [2]School of Physical Science and Technology, Guangxi University, Nanning, China | [3]Department of Materials Science and Engineering, National University of Singapore, Singapore | [4]Sensor Laboratory, Department of Information Engineering, University of Brescia, Brescia, Italy

Correspondence: Elisabetta Comini (elisabetta.comini@unibs.it) | Daniel H. C. Chua (danielchua@nus.edu.sg) | Pooi See Lee (pslee@ntu.edu.sg)

Received: 3 March 2025 | **Revised:** 4 July 2025 | **Accepted:** 3 September 2025

Funding: This work was supported by A*STAR-MAECI Joint Grant Call–Scientific and Technological Cooperation Grant, Award No. R23I0IR039 and in part by the Italian Ministry of Foreign Affairs and International Cooperation, Grant number SG23GR06.

Keywords: cathode | oxygen reduction reaction | perovskite oxide | SOFC

ABSTRACT

Solid oxide fuel cells (SOFCs) represent an advanced technology for achieving effective energy conversion, offering high efficiency and fuel flexibility. Perovskite-type oxide cathode materials are critical to their operation, due to their excellent electrochemical performance. Doping strategies are commonly employed to improve their physicochemical and electrochemical characteristics. However, the precise role of high-valence dopants in modulating oxygen reduction reaction (ORR) activity and oxygen ion transport remains inadequately understood. This study investigates the B-site engineering in the perovskite material $Pr_{0.4}Sr_{0.6}Co_{0.2}Fe_{0.8}O_{3-\delta}$ (PSCF) through niobium (Nb) doping, in which iron (Fe) is partially substituted to elucidate the influence of Nb on cathode performance. Density functional theory (DFT) calculations reveal that doping significantly reduces the oxygen vacancy formation energy (E_{vac}) at Co/Fe-related sites, thus promoting oxygen vacancy generation and enhancing oxygen mobility in the lattice. In contrast, the E_{vac} at Nb-related sites increases, indicating a site-dependent redistribution of oxygen defects and local charge compensation. This redistribution facilitates the ORR pathway associated with high valence Co^{4+}/Fe^{4+} species at intermediate temperatures, even though the high temperature ORR involving Co^{3+}/Fe^{3+} may be partially suppressed. As the Nb content increases, a decrease in polarization resistance is observed, with the optimal electrochemical performance achieved in $PSCFN_{0.05}$ and $PSCFN_{0.1}$, showing polarization resistances of 0.052 and 0.050 Ω cm^2, respectively. Notably, $PSCFN_{0.1}$ achieves more than 2.6 times the power density of the undoped PSCF at 500°C (77 vs. 29 mW·cm^{-2}). These findings provide fundamental insights into rational B-site design, offering a clear strategy for enhancing the catalytic activity and ion transport properties of perovskite cathodes in SOFCs.

1 | Introduction

Solid oxide fuel cells (SOFCs) have attracted significant attention as a promising technology for clean and efficient energy conversion [1–5]. These electrochemical devices operate at high temperatures and offer a range of advantages, including high efficiency, fuel flexibility, and low environmental impact [6–9]. The cathode plays a crucial role in determining the overall performance of SOFCs, as it is responsible for the oxygen reduction reaction (ORR), which involves the reduction of oxygen

molecules to oxygen ions that are subsequently transported through the electrolyte to the anode [10, 11]. Therefore, the development of high-performance cathode materials with superior oxygen reduction kinetics and stability is critical for the advancement of SOFC technology.

Among the various materials explored, perovskite-type oxides are widely used as SOFC cathode materials because of their favorable mixed ionic and electronic conductivity, oxygen vacancy formation capability, and high chemical stability at elevated temperatures [12–14]. Manganese-based oxides ($La_{1-x}Sr_xMnO_{3-\delta}$) [15]; iron-based oxides ($SrFeO_{3-\delta}$) [16]; cobalt-based oxides ((La, Sr)$CoO_{3-\delta}$) [17], $Sr_2(Co_{1+x}, Mo_{1-x})O_{6-\delta}$ [18], and $LnBaCo_2O_{5+\delta}$) [19]; and mixed transition metal (TM) oxides, such as La(Ni, Fe)$O_{3-\delta}$ and Sr(Co, Fe)$O_{3-\delta}$, have effectively enabled SOFC operation at intermediate temperatures (600–800°C) [20–22], reducing the typical operating temperature from the original 800–1000°C. Those perovskite-type oxides with the single perovskite (ABO_3) or double perovskite ($A_2B'B''O_6$) structure offer flexibility in compositional tuning, where A-site and B-site elements can be selectively doped to modulate electrochemical performance [23, 24]. Generally, the A-site is occupied by larger alkaline-earth or rare-earth metal elements, such as barium (Ba), strontium (Sr), or lanthanum (La) [12, 25, 26], while the B-site is typically populated with transition metals like cobalt (Co), manganese (Mn), and iron (Fe) [3, 27]. Adjusting the A-site composition can modify the lattice parameters and thermal expansion coefficients (TECs), thereby influencing the material's chemical stability and overall conductivity [28, 29]. Ren's study indicates that in the $Ln_{0.8}Sr_{0.2}FeO_{3-\delta}$ series, as the ionic radius of the A-site cation decreases, the electronic conductivity decreases primarily due to increased crystal structure asymmetry [30]. Additionally, smaller A-site cations enhance the material's reactivity with yttria-stabilized zirconia (YSZ), affecting its stability. B-site doping is particularly effective in modulating the oxygen vacancy concentration and formation energy, which is crucial for improving oxygen ion mobility within the lattice and subsequently enhancing ORR performance [16, 31, 32]. Cu-doping in $Ba_{0.5}Sr_{0.5}Fe_{1-x}Cu_xO_{3-\delta}$ reduces oxygen vacancy formation energy, enhances charge redistribution around dopant sites, and decreases the activation barrier for oxygen diffusion, ultimately improving the ORR activity [24]. Doping with high-valence elements such as Ti^{4+}, Nb^{5+}, and Mo^{6+} in $La_{0.5}Sr_{0.5}FeO_{3-\delta}$ materials has been found to promote oxygen vacancy formation [23]. Nb doping optimizes oxygen vacancy formation energy and surface reaction kinetics to enhance the ORR activity of $SrFe_{0.9}Nb_{0.1}O_{3-\delta}$, enabling the composite electrode to achieve a peak power density of 502 mW cm^{-2} at 700°C [33, 34].However, the mechanism by which these dopants affect ORR activity remains insufficiently understood, particularly regarding their site-specific effects on oxygen vacancy energetics and local electronic structure. Understanding the interplay between dopant valence, defect distribution, and catalytic activity is critical for the rational design of high-performance cathodes. In this context, the Fe-Co-based perovskite systems, $Pr_{1-x}Sr_xFe_{1-y}Co_yO_{3-\delta}$ has recently gained attention as a promising cathode material due to its favorable electrochemical characteristics [13]. The incorporation of Pr^{3+} at the A-site facilitates additional electronic conduction pathways through Pr^{3+}/Pr^{4+} redox transitions, enhancing overall conductivity and reducing activation losses. Notably, the composition with Co content $y = 0.2$ achieves an effective balance between electronic conductivity and catalytic activity, making it an ideal platform for further performance optimization via B-site modification [35]. These features make PSCF an ideal platform for further optimization through B-site modification.

In this study, we investigate the effect of Nb^{5+} doping at the B-site of PSCF to clarify its influence on oxygen vacancy formation and ORR performance. Nb partially replaces Fe to modulate oxygen defect chemistry in a site-dependent manner. Density functional theory (DFT) calculations reveal that Nb doping significantly lowers the E_{vac} at Co/Fe-related sites, thereby promoting oxygen vacancy generation and enhancing lattice oxygen mobility. Experimentally, O_2-temperature-programmed desorption (O_2-TPD) results show broadened desorption peaks and increased oxygen release intensity for Nb-doped samples, suggesting enhanced surface oxygen exchange. Electrochemical impedance spectroscopy (EIS) confirms that polarization resistance (R_p) decreases with moderate Nb doping: $PSCFN_{0.05}$ and $PSCFN_{0.1}$ exhibit R_p values of 0.052 and 0.050 Ω·cm^2 at 800°C, respectively, compared to 0.188 Ω·cm^2 for undoped PSCF. In single-cell tests at 500°C, $PSCFN_{0.1}$ delivers a peak power density of 77 mW·cm^{-2}—2.6 times that of PSCF (29 mW·cm^{-2}). Distribution of relaxation times (DRT) analysis further reveals that Nb incorporation accelerates multiple ORR steps, including oxygen adsorption, dissociation, and surface diffusion. However, excessive doping ($PSCFN_{0.15}$ and $PSCFN_{0.2}$) leads to a slight increase in E_{vac} and a reduction in the number of active Co/Fe sites, resulting in performance degradation. These findings highlight that optimized Nb doping levels (5–10 mol%) enable a favorable balance between oxygen defect formation and active site availability, promoting ORR activity without compromising structural stability. This work provides a mechanistic understanding of how Nb doping modulates oxygen vacancy behavior in PSCF and demonstrates the effectiveness of B-site engineering in designing high-performance perovskite cathodes for intermediate-temperature SOFCs.

2 | Results and Discussion

As shown in Figure 1A, B-site Nb substitution was employed to investigate its effects on the ORR activity of PSCF as a cathode material for SOFC. Building upon the PSCF perovskite-type structure, Nb was introduced to partially substitute Fe atoms at the B-site, with systematic variations in Nb content resulting in the formations of PSCF, $PSCFN_{0.05}$, $PSCFN_{0.1}$, $PSCFN_{0.15}$, and $PSCFN_{0.2}$, allowing for an investigation of the doping effects. The desired materials were synthesized using the sol-gel sintering method (Figure 1B), which allows for precise control over the composition and homogeneity of the resulting perovskite structure and reduces the temperature required for the sintering process. As illustrated in Figure 1C, the obtained cathode powders with varying doping levels exhibit similar surface morphologies and uniform particle distributions. Compared to undoped PSCF (Figure S1A), Nb-doped samples display a general increase in particle size, with particle dimensions enlarging progressively with higher Nb substitution. Figure S1C shows that EDS analysis of the $PSCFN_{0.1}$ powder reveals an even distribution of elements. And quantitative particle size distribution analysis was performed based on SEM images (Figure S2). The calculated average particle sizes—determined from 45 particles per sample—are 127.8 ± 50 nm for PSCF, 139.4 ± 58 nm for $PSCFN_{0.1}$,

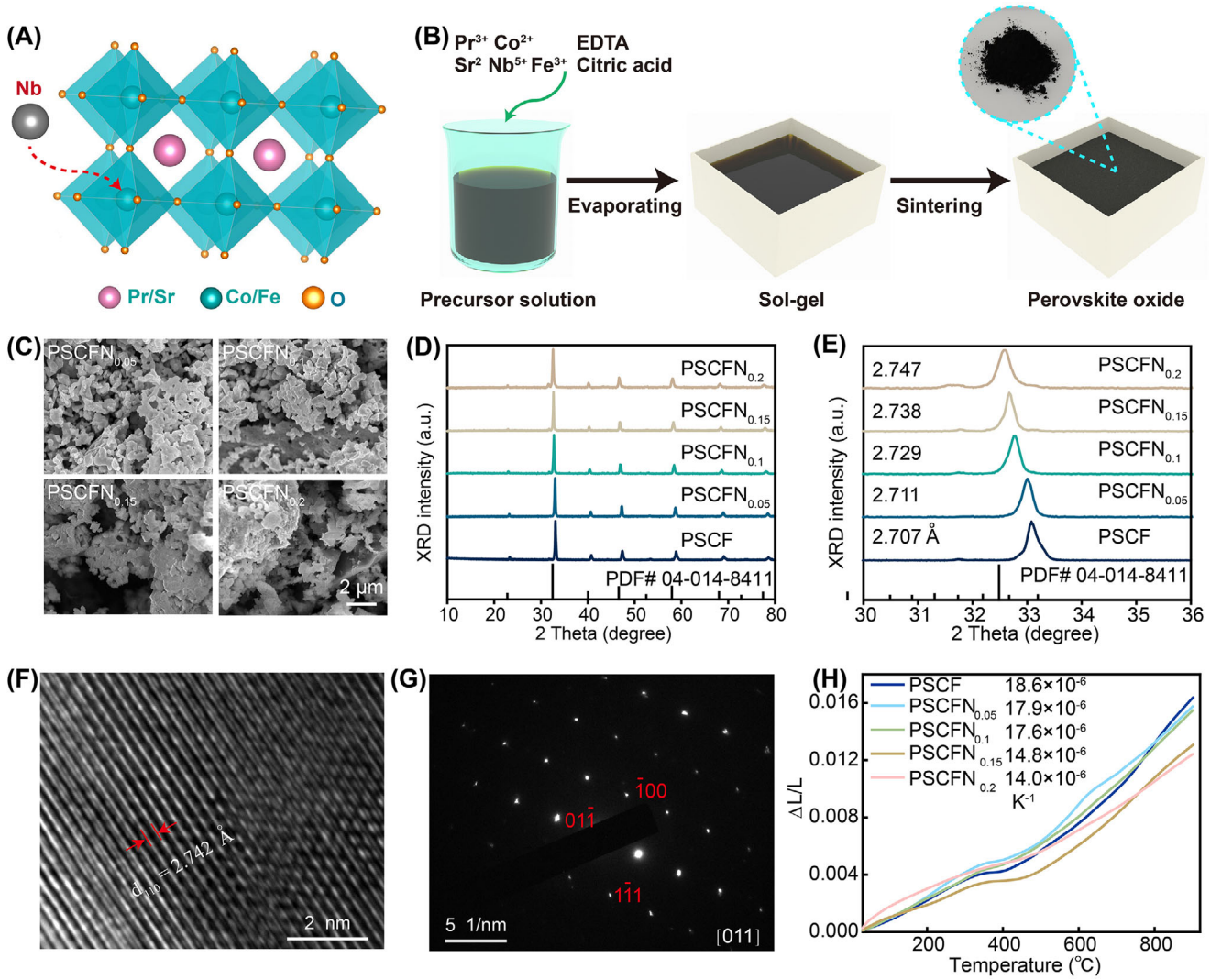

FIGURE 1 | B-site engineering strategy for perovskite oxides. (A) Schematic of B-site engineering strategy. (B) Sol-gel synthesis process. (C) SEM images of Nb-doped samples. (D) XRD patterns of PSCF and Nb-doped samples. (E) Magnified view of main XRD peak shifts. (F) HRTEM image of $PSCFN_{0.2}$. (G) SAED pattern of $PSCFN_{0.2}$. (H) Thermal expansion curves of cathodes.

and 137.0 ± 50 nm for $PSCFN_{0.2}$. This trend suggests that Nb doping facilitates growth of particles, due to altered solid-phase reaction kinetics during sintering induced by Nb incorporation. Furthermore, Figure 1D displays X-ray diffraction (XRD) patterns of the cathode powders, all of which exhibit characteristic peaks of the typical perovskite phase. The diffraction peaks maintaining similar distributions and show good agreement with the standard perovskite phase of $Sr_{0.5}Pr_{0.5}FeO_{2.75}$ (PDF# 04-014-8411), which adopts a cubic perovskite structure (Pm-3m). However, given the partial substitution with Co and Nb, the actual structure of PSCF and PSCFN is more likely to be slightly distorted from the ideal cubic phase, possibly exhibiting orthorhombic or pseudocubic symmetry. And, as Nb concentration increases, a shift of the diffraction peaks to lower angles is observed. Taking the (110) reflection as an example (Figure 1E), the corresponding d-spacing increases from 2.707 to 2.747 Å, suggesting lattice expansion. This is similar to the effect observed with high-valence ion doping in $La_{0.5}Sr_{0.5}FeO_{3-\delta}$ [23]. In addition, the average crystallite sizes calculated using the Scherrer equation are 33.9 nm for PSCF, 34.8 nm for $PSCFN_{0.05}$, 36.2 nm for $PSCFN_{0.1}$, 36.15 nm for $PSCFN_{0.15}$, and 29.3 nm for $PSCFN_{0.2}$. The increase in crystallite size at moderate Nb levels indicates the promotion of crystal growth, while the decrease at $PSCFN_{0.2}$ may be related to local distortion or phase strain at higher substitution levels. Transmission Electron Microscopy (TEM) analysis was employed to gain further insight into the structural features of the Nb-doped perovskite. As shown in Figure 1F, the high-resolution TEM (HRTEM) image of the $PSCFN_{0.2}$ sample reveals distinct lattice fringes with an interplanar spacing of 2.742 Å, which corresponds to the (110) plane of the cubic perovskite lattice. And the selected-area electron diffraction (SAED) pattern in Figure 1G displays sharp and regularly arranged diffraction spots that are indicative of a pseudocubic perovskite structure and are approximately consistent with the Pm-3m space group when viewed along the [011] zone axis, confirming the formation of a well-crystallized. Figure 1H illustrates the impact of Nb doping on the thermal expansion behavior of PSCF-based cathodes from 30–900°C. The extracted (thermal expansion coefficient) TEC shows that the undoped PSCF sample has a TEC of 18.6×10^{-6} K^{-1}. Nb doping results in progressively lower TECs: 17.9×10^{-6} K^{-1}

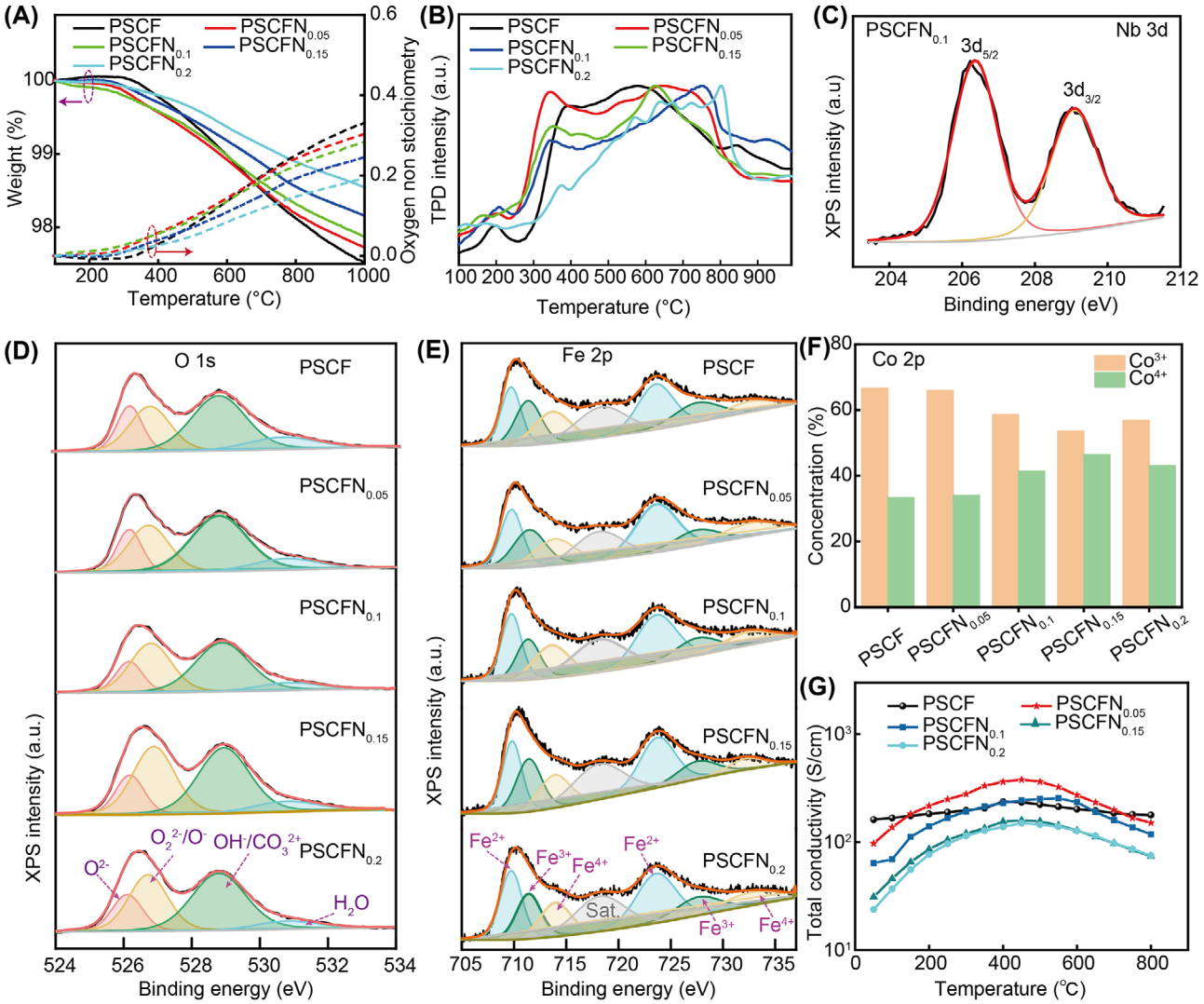

FIGURE 2 | Thermal stability and surface chemistry analysis. (A) TGA and (B) O_2-TPD spectra of cathode powders. XPS spectra of (C) Nb 3d in $PSCFN_{0.1}$ and (D) O 1s and (E) Fe 2p for all cathodes. (F) Distribution of Co^{3+} and Co^{4+} concentrations perovskite oxides. (G) Conductivity curves of cathodes.

for $PSCFN_{0.05}$, 17.6×10^{-6} K^{-1} for $PSCFN_{0.1}$, 14.8×10^{-6} K^{-1} for $PSCFN_{0.15}$, and 14.0×10^{-6} K^{-1} for $PSCFN_{0.2}$. Although slight increases in thermal expansion were observed for $PSCFN_{0.05}$ and $PSCFN_{0.1}$ in the low to mid-temperature range, the overall TEC still decrease progressively with higher Nb content. Notably, the significantly reduced TEC of $PSCFN_{0.15}$ and $PSCFN_{0.2}$ matched well with common electrolyte materials like YSZ ($\sim 10 \times 10^{-6}$ K^{-1}) [36] and gadolinium-doped ceria (GDC; $\sim 11 \times 10^{-6}$ K^{-1}) [37], enhancing thermal compatibility and improving thermal cycling stability in SOFC.

To examine the effect of Nb doping on the thermal stability of PSCF and the thermal reduction behavior of B-site ions, a series of analyses including thermogravimetric analysis (TGA), Oxygen Temperature-Programmed Desorption (O_2-TPD), and X-ray photoelectron spectroscopy (XPS) were conducted. As shown in Figure 2A, the TGA results demonstrate that all synthesized powders maintain structural stability over the temperature range of 100°C to 1000°C. Notably, Nb doping results in greater mass loss below 600°C, indicating the presence of additional nonstoichiometric oxygen (δ) at lower temperatures. Notably, at 600°C, the δ values are 0.133 (PSCF), 0.144 ($PSCFN_{0.05}$), 0.136 ($PSCFN_{0.1}$), 0.109 ($PSCFN_{0.15}$), and 0.084 ($PSCFN_{0.2}$). Figure 2B provides insight into the oxygen desorption characteristics of Nb-doped PSCF powders, revealing distinct oxygen desorption peaks. Two types of oxygen desorption behaviors are observed in the perovskite oxides [38]. The first type, α-O desorption (300°C–600°C), corresponds to the thermal reduction of tetravalent TM ions at the B-site to trivalent state. The α_1O desorption peak, observed between 300°C–450°C, corresponds to the reduction of Co^{4+} to Co^{3+}, while the α_2-O desorption, occurring between 450°C–600°C, is associated with the reduction of Fe^{4+} to Fe^{3+}. This process is represented by the following reaction:

$$2B_B^{\cdot} + O_O^{\times} = 2B_B^{\times} + V_{\ddot{O}} + \frac{1}{2}O_2 \quad (1)$$

where $B_B^{\cdot}$ an $B_B^{\times}$ ions represent Co^{4+}/Fe^{4+} and Co^{3+}/Fe^{3+}, respectively [27, 39]. Nb-doped samples ($PSCFN_{0.05}$, $PSCFN_{0.1}$, and $PSCFN_{0.15}$) exhibit a broadened desorption peak in this range,

with a slight shift of the α_1-O desorption peak toward lower temperatures. This shift suggests that appropriate levels of Nb doping reduces the energy barrier for oxygen desorption, enhancing the perovskite oxygen exchange rate, which could be beneficial for oxygen ion transport and catalytic efficiency. Moreover, this also explains the greater weight loss observed in TGA for Nb-doped PSCF in the 300–600°C range compared to undoped PSCF (Figure 2A). The Nb doping lowers the activation energy for the reduction of Co^{4+}/Fe^{4+} to Co^{3+}/Fe^{3+}, facilitating this process and resulting in a higher concentration of oxygen vacancies at low to intermediate temperatures. The second type, β-O desorption (> 700°C), represents the high-temperature desorption associated with the further reduction of trivalent transition metal ions (Co^{3+}/Fe^{3+}) to divalent states (Co^{2+}/Fe^{2+}), leading to the release of lattice oxygen. This process is described by the reaction:

$$2B_B^{\times} + O_O^{\times} = 2B_B' + V_{\ddot{O}} + \frac{1}{2}O_2 \quad (2)$$

where $B_B^{'}$ represents Co^{2+}/Fe^{2+} ions. The data show that with increasing Nb doping concentration, particularly in the $PSCFN_{0.2}$, the β-O desorption is enhanced, indicating a greater release of lattice oxygen at high temperatures. However, $PSCFN_{0.2}$ also exhibits a reduction in α-O desorption in the lower temperature region, suggesting that excessive Nb doping may inhibit oxygen vacancy formation in the lower temperature region, potentially altering the balance between lattice oxygen mobility and vacancy-mediated oxygen transport. And the PSCF exhibits the highest overall weight loss, with a significant portion occurring at elevated temperatures (above ~600°C), which can be attributed to the reduction of trivalent B-site cations (Fe^{3+}/Co^{3+}) to their divalent states.

Following Nb substitution (Nb^{5+}: 0.64 Å) for Fe (Fe^{4+}: 0.585 Å, Fe^{3+}: 0.64 Å, Fe^{2+}: 0.78 Å), the higher oxidation state of Nb induces a charge redistribution among the B-site ions. This electronic compensation mechanism leads to adjustments in the oxidation states of Fe and Co, and induces lattice distortion, which in turn impacts oxygen vacancy formation behavior. Using the $PSCFN_{0.1}$ as an example, Figure 2C presents the XPS fitting spectra of Nb 3d, highlighting the Nb^{5+} peaks at 206.4 and 209.1 eV [16, 39]. This charge redistribution significantly influences the oxygen environment, as evidenced by the O 1s spectra (Figure 2D). With increasing Nb content, the proportion of lattice oxygen (O^{2-}) decreases, while the concentration of surface-adsorbed oxygen species (O_2^{2-}/O^-) increases [13, 40]. Specifically, the O_2^{2-}/O^-content rises from 26.91% in PSCF to 35.53% in $PSCFN_{0.15}$, as shown in Table S1. This suggests that Nb doping significantly influences the electronic and structural properties of the PSCF, and enhances the oxygen adsorption capacity, which can be beneficial for catalytic activity. This is further supported by the Fe 2p spectra (Figure 2E), which reveal the presence of Fe^{2+}, Fe^{3+}, and Fe^{4+} oxidation states [41]. With increasing Nb doping, leading to a decrease in the average Fe valence, from +2.82 in PSCF to +2.73 in $PSCFN_{0.15}$, as detailed in Table S2. This suggests that Nb doping stabilizes lower Fe oxidation states, contributing to lattice expansion, which is consistent with the XRD results [42]. The lattice distortion caused by Nb doping alters the bonding interactions between the B-site cations and the surrounding oxygen anions, thereby influencing the E_{vac}. The Co 2p XPS spectra (Figure S3) show characteristic peaks at ~780.3 and ~795.2 eV for Co^{3+}, and at 781.8 and 796.3 eV for Co^{4+} [40]. With increasing Nb doping, the proportion of Co^{3+} decreases from 66.7% (PSCF) to 53.6% ($PSCF_{0.15}$), while the proportion of Co^{4+} increases from 33.3% to 46.4%. This trend indicates that Nb doping stabilizes Co in a higher oxidation state, suggesting a redistribution of charges that leads to structural distortion within the lattice. Such charge redistribution and the associated lattice and electronic structure modulation exert a profound influence on the defect chemistry and charge transport properties, thereby governing the temperature-dependent conductivity behavior of the Nb-doped cathodes. As depicted in Figure 2G, all cathodes demonstrate characteristic thermally activated conduction behavior, with total conductivity initially increasing and subsequently decreasing as the temperature rises. In the intermediate temperature range (400–600°C), the conductivity of $PSCFN_{0.05}$ and $PSCFN_{0.1}$ is higher than that of undoped PSCF, with $PSCFN_{0.05}$ achieving a peak conductivity of 379 S·cm^{-1} at 450°C. This enhancement is primarily attributed to the elevated concentration of oxygen vacancies and enhanced oxygen ion mobility facilitated by moderate Nb doping. Supporting evidence from TGA and O_2-TPD analyses indicates that Nb doping reduces the activation energy required for Co^{4+}/Fe^{4+} reduction, thereby promoting oxygen desorption and vacancy formation at intermediate temperatures. In contrast, within the low-temperature region, the conductivity of Nb-doped samples is lower than PSCF, signifying a reduction in electronic conductivity. This decline is attributed to the substitution of redox-active Fe/Co ions with redox-inactive Nb^{5+}, which disrupts the electron hopping mechanisms between Co^{4+}/Co^{3+} and Fe^{4+}/Fe^{3+} redox couples. At higher doping levels (≥0.15), the overall conductivity decreases across the entire temperature range, likely due to pronounced lattice distortion and an imbalanced oxygen vacancy distribution, both of which impede efficient charge carrier transport.

Vienna Ab initio Simulation Package (VASP) was employed to perform first-principles calculations to investigate the influence of Nb doping on the ORR [24, 43–45]. In the simulation model, the energy differences between the three Co arrangement configurations within the PSCF structure are found to be negligible, as shown in Figure S4. To optimize computational efficiency, the bulk contraposition arrangement of Co was selected for further simulation. Simulations were conducted on the (001) surface with lower surface energy [12]. As illustrated in Figure 3A,B, the B-site cations (Fe1, Fe2, Fe3, Co, and Nb) serve as active sites for oxygen adsorption, while V1, V2, V3, and V4 denote the locations where oxygen vacancies are introduced. The simulated results presented in Table 1 demonstrate that with Nb incorporation, the surface E_{vac} at the Co-$V_{\ddot{O}}$-Fe1 and Fe1-$V_{\ddot{O}}$-Fe2 sites decrease from 2.04 and 2.08 eV to 1.89 and 1.93 eV, respectively. Similarly, the bulk E_{vac} decreased from 2.41 and 2.55 eV to 1.68 and 2.18 eV, resulting in an overall reduction in the average vacancy formation energy. Since oxygen ion transport in perovskite oxides occurs via a vacancy hopping mechanism, lower E_{vac} corresponds to a higher concentration of oxygen vacancies. The substitution of Fe with Nb increases vacancy concentration, enhancing pathways for oxygen ion migration and ultimately improving the ion transport properties in PSCF. However, the E_{vac} increases at certain sites, such as Fe2-$V_{\ddot{O}}$-Nb and Nb-$V_{\ddot{O}}$-Co (rising to 2.68 and 3.14 eV in the bulk, respectively), suggesting that Nb-associated regions may inhibit vacancy formation locally and potentially impede ion transport. This finding implies that moderate Nb doping

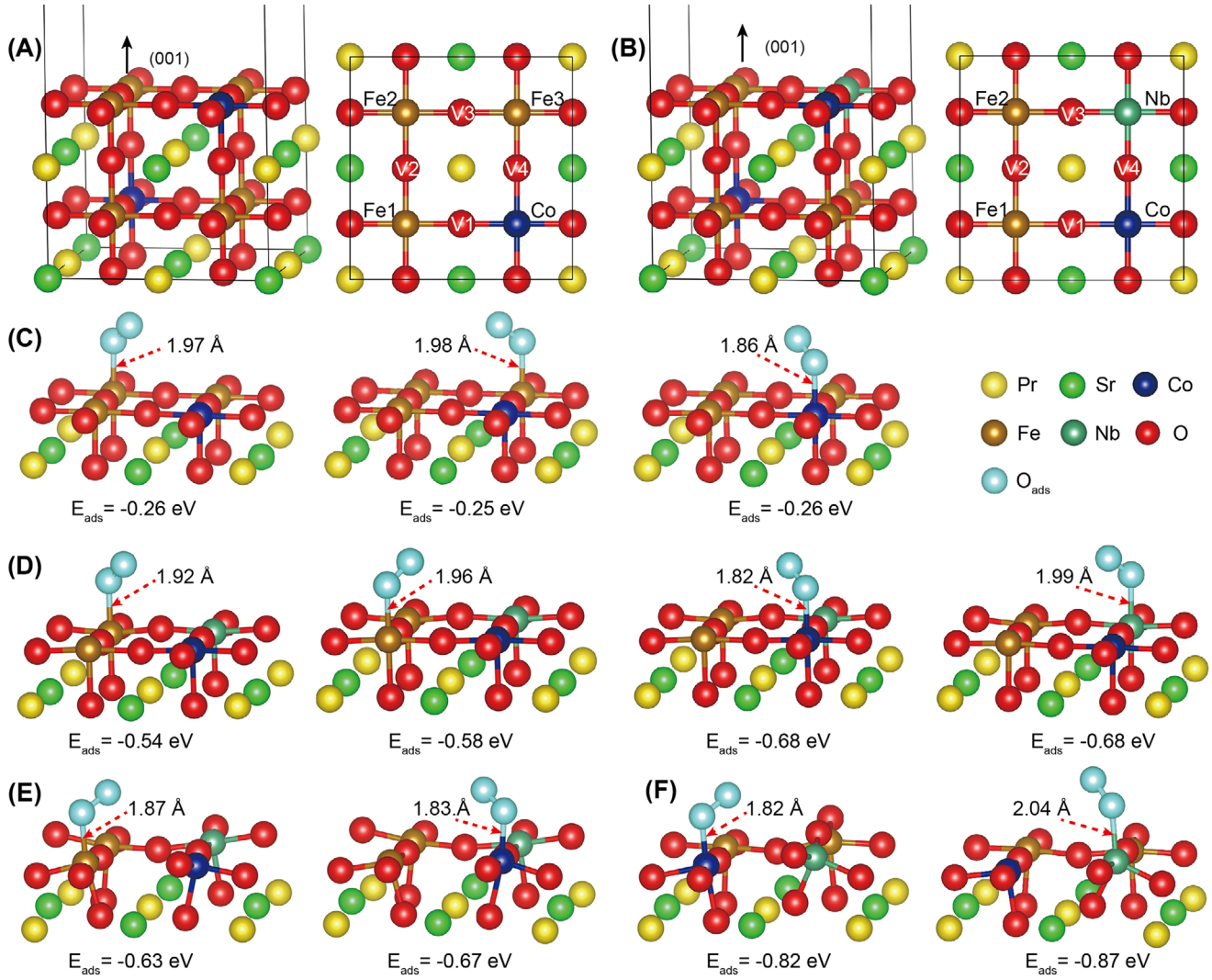

FIGURE 3 | Simulation of oxygen adsorption capability. Perfect PSCF (A) and PSCFN (B) (001) surfaces with corresponding top views. V1, V2, V3, and V4 represent potential oxygen vacancy positions. Oxygen adsorption on the optimized structures of the perfect PSCF (C) and PSCFN (D) (001) surfaces, along with the bond length between the adsorbed oxygen and the active cation, and the corresponding E_{ads}. Oxygen adsorption on the PSCFN surface with vacancies Co-$V_{Ö}$-Fe1 (E) and Co-$V_{Ö}$-Nb (F).

TABLE 1 | Oxygen vacancy formation energy.

Position	Surface E_{vac}	bulk E_{vac}
PSCF		
Co-$\mathbf{V}_{Ö}$-Fe1	2.04 eV	2.41 eV
Fe1-$\mathbf{V}_{Ö}$-Fe2	2.08 eV	2.55 eV
PSCFN		
Co-$\mathbf{V}_{Ö}$-Fe1	1.89 eV	1.68 eV
Fe1-$\mathbf{V}_{Ö}$-Fe2	1.93 eV	2.18 eV
Fe2-$\mathbf{V}_{Ö}$-Nb	2.54 eV	2.68 eV
Nb-$\mathbf{V}_{Ö}$-Co	2.24 eV	3.14 eV

promotes ion transport by increasing the vacancy concentration, provided that enough active Co/Fe sites is maintained. However, excessive Nb doping, which results in more Nb-associated sites, may restrict oxygen ion mobility by locally stabilizing the lattice and limiting vacancy formation and ion transport efficiency. This observation also aligns with TGA results, as Nb content increases, the weight loss of the cathode powder during heating decreases, reflecting a reduction in oxygen vacancy formation within the lattice. On the perfect PSCF (001) surface (Figure 3C), the B-site metals (Fe1, Fe2, Fe3, and Co) show relatively high E_{ads} values, indicating a limited oxygen adsorption capacity. In PSCFN (Figure 3D), Nb doping enhances oxygen adsorption by lowering the E_{ads} (with higher absolute values), with values of −0.54, −0.58, −0.68, and −0.68 eV at the Fe1, Fe2, Nb, and Co sites, respectively. Upon introducing a Co-$V_{Ö}$-Fe1 defect (show in Table 2), the Co site in PSCF exhibits the most negative adsorption energy at −1.05 eV, indicating the strongest oxygen adsorption capacity on this defective surface, with a slightly shorter bond length (1.87 Å). Fe1 and Fe2 sites also show reduced E_{ads}, suggesting that the formation of oxygen vacancies enhances the oxygen adsorption capacity across the PSCF surface. However, the Fe3 site displays positive adsorption energy (0.61 eV), indicating reduced stability

TABLE 2 | Adsorption capacity of PSCF and PSCFN (001) surfaces.

Species		Fe1	Fe2	Fe3/Nb	Co
Perfect PSCF (001) surface	E_{ads} (eV)	−0.25	−0.26	−0.25	−0.26
	Bond length (Å)	1.98	1.97	1.98	1.86
Defective PSCF (001) surface (Co-$\mathbf{V}_{\ddot{O}}$-Fe1)	E_{ads} (eV)	−0.69	−0.46	0.61	−1.05
	Bond length (Å)	1.85	1.92	1.97	1.87
Perfect PSCFN (001) surface	E_{ads} (eV)	−0.58	−0.54	−0.68	−0.68
	Bond length (Å)	1.96	1.92	1.99	1.82
Defective PSCFN (001) surface (Co-$\mathbf{V}_{\ddot{O}}$-Fe1)	E_{ads} (eV)	−0.63	−0.35	−0.50	−0.67
	Bond length (Å)	1.87	1.95	1.83	2.18
Defective PSCFN (001) surface (Nb-$\mathbf{V}_{\ddot{O}}$-Co)	E_{ads} (eV)	−0.65	0.12	−0.87	−0.82
	Bond length (Å)	1.86	1.79	2.04	1.82

for oxygen adsorption and even a repulsive interaction near this vacancy. For the equivalent vacancy introducing in PSCFN (Figure 3E), the E_{ads} at Fe1 and Nb sites are −0.63 and −0.50 eV, respectively, showing enhanced adsorption capacity, although their absolute values are lower than in PSCF. However, with the introduction of Nb-$V_{\ddot{O}}$-Co defects on the PSCFN surface (Figure 3F), the Co and Nb sites demonstrate E_{ads} of −0.82 and −0.87 eV, respectively, all of which show strong adsorption capacity. This indicates that the presence of oxygen vacancies near Nb significantly enhances the oxygen adsorption capacity of Fe and Co active sites, thereby improving the overall oxygen adsorption capability of PSCFN relative to PSCF. Such improvement can be attributed to the modification of the surface electronic structure induced by Nb, which facilitates stronger interactions with oxygen species. The energy profiles in Figures S5 and S6 provide further insights into the effects of Nb doping on the oxygen adsorption and dissociation processes in PSCF-based cathodes. Upon adsorption, oxygen molecules interact with active B-site cations, subsequently migrating toward oxygen vacancy sites, where they undergo dissociation into atomic oxygen, followed by incorporation into the lattice or facilitation of oxygen ion diffusion pathways. On the undoped PSCF surface, oxygen adsorption and dissociation exhibit moderate energy barriers, with Co-$V_{\ddot{O}}$-Fe1 vacancy sites playing a significant role in facilitating these processes. However, with Nb incorporation in PSCFN, these processes become significantly more thermodynamically favorable. Notably, after dissociative adsorption, the energy of the oxygen species stabilized at Co-$V_{\ddot{O}}$-Nb sites is highly exergonic, reaching −4.51 eV. This indicates that Nb doping enhances the stabilization of oxygen species, particularly at defect sites. Nevertheless, the strong adsorption of oxygen at Nb-related sites may indicate excessive stabilization of oxygen species, which could hinder their further diffusion and reduce oxygen mobility. Therefore, Nb incorporation lowers E_{vac} and E_{ads} at most sites, enhancing oxygen vacancy formation and surface reactivity. However, excessive doping leads to strongly stabilized Nb-associated regions, which may impede oxygen vacancy mobility and ion transport. These findings emphasize the importance of optimizing Nb doping levels to balance oxygen adsorption, vacancy concentration, and lattice dynamics for optimal electrochemical performance. In addition to vacancy formation and oxygen adsorption energy calculations, site-resolved projected density of states (PDOS) was analyzed to further understand the Nb-induced electronic modulation. As shown in Figures S7–S9, Nb^{5+} substitution at the Fe3 site results in a downward shift of the Fe 3d states (particularly Fe1, Fe2, Fe4–Fe6), along with reduced Fermi-level density, indicating partial reduction of Fe^{4+}/Fe^{3+} to Fe^{2+} and enhanced electron localization. Co1 and Co2 also exhibit slightly suppressed 3d states near the Fermi level, consistent with $Co^{3+}$to Co^{4+} transition. These electronic shifts reflect a Nb-driven charge compensation mechanism, consistent with the lower E_{vac} and enhanced oxygen adsorption observed at these B-site cations. Notably, the 4d states of Nb are positioned well above the Fermi level, confirming that Nb does not contribute to electronic conduction but modulates the surrounding electronic environment, facilitating vacancy formation and surface reactivity. Therefore, PDOS analysis provides essential support for understanding how Nb doping enhances ORR activity in PSCF cathodes by regulating the B-site electronic structure.

To further investigate the potential of Nb-doped PSCF as cathodes for SOFC, symmetrical cells were employed to evaluate their electrochemical properties. This approach allows for a detailed assessment of the ORR performance, providing insight into the material's conductivity, and catalytic activity for SOFC applications. Figure 4 presents the EIS performance depicting the temperature-dependent impedance response of symmetrical cells with perovskite oxide-based cathodes, measured at 500°C, 600°C, 700°C, and 800°C. The Nyquist plots exhibit characteristic semicircular arcs, corresponding to the polarization resistance R_p of the symmetrical cells. All the symmetrical cells equivalent circuit for EIS fitting (Figure S10) shows two distinct arcs at 500–600°C and a merged arc at 700–800°C due to accelerated electrochemical processes. For the electrode with lower Nb doping levels, R_p values are significantly reduced compared to higher doping cathode material, especially at low temperatures. For instance, at 500°C, the R_p is 11.08 Ω cm^2 for $PSCFN_{0.1}$, 14.03 Ω cm^2 for $PSCFN_{0.05}$, and 15.29 Ω cm^2 for $PSCFN_{0.15}$, which are significantly lower than the values of 22.47 Ω cm^2 for $PSCFN_{0.2}$, further demonstrating the superior performance of moderate Nb doping in lowering R_p. And the corresponding ohmic resistances of these symmetrical cells with different cathode materials are summarized in Table S3, showing similar electrolyte thicknesses (~600 μm) across all samples. In comparison, the undoped PSCF

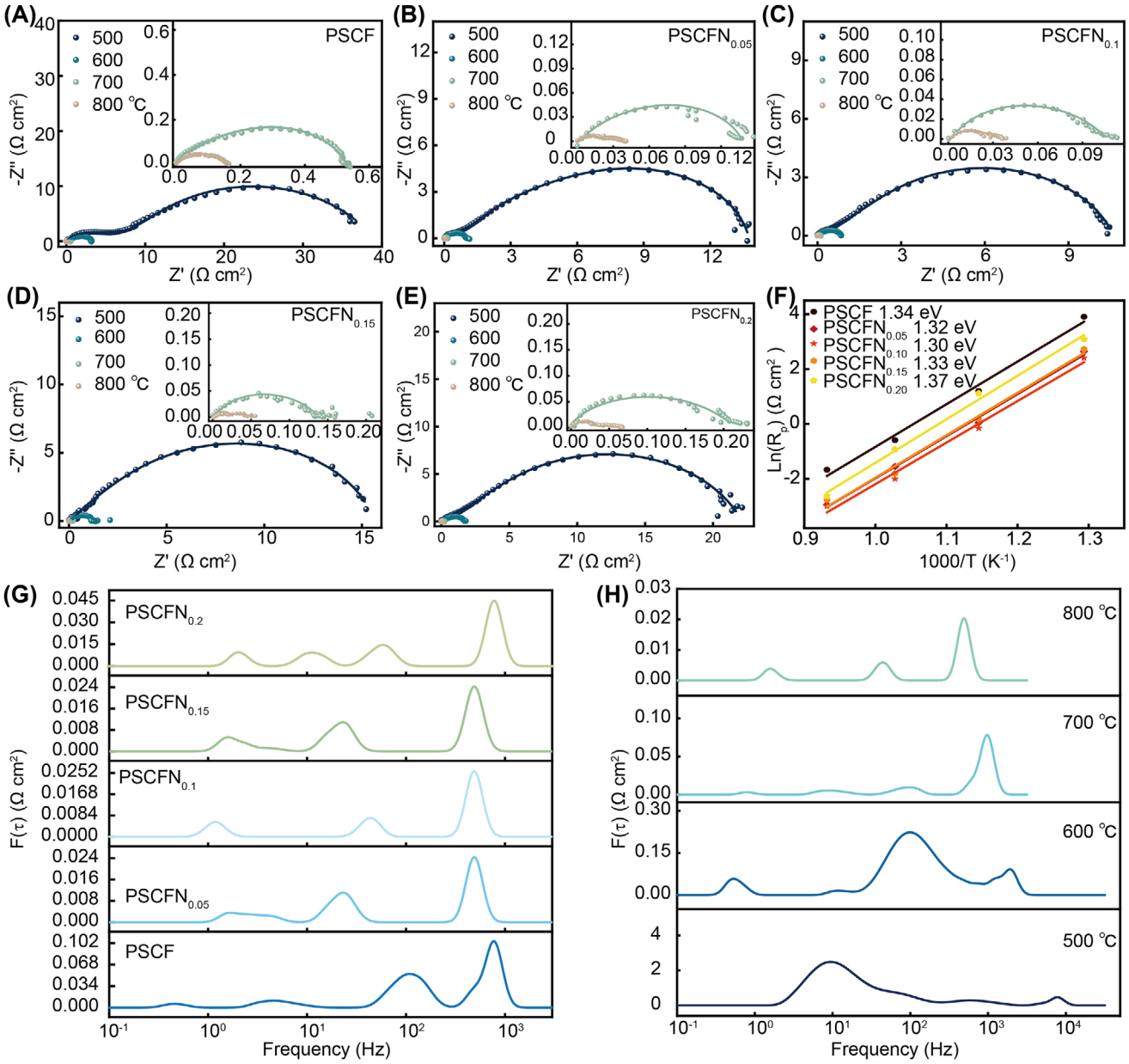

FIGURE 4 | EIS and DRT analysis of PSCF and Nb-doped PSCF materials. Nyquist plots of PSCF and PSCFN at different temperatures (500–800°C) for various Nb-doping levels: (A) PSCF, (B) $PSCFN_{0.05}$, (C) $PSCFN_{0.1}$, (D) $PSCFN_{0.15}$, (E) $PSCFN_{0.2}$. (F) Arrhenius plots of polarization resistance. (G) DRT spectra of PSCF and Nb-doped PSCF at 800°C. (H) DRT spectra of $PSCFN_{0.1}$ at 500– 800°C.

sample exhibits a much higher R_p of 49.69 Ω cm^2 at the same temperature. And this trend persists at 800°C, with $PSCFN_{0.05}$ and $PSCFN_{0.1}$ showing the best performance, achieving an R_p of 0.052 and 0.050 Ω·cm^2, respectively. While $PSCFN_{0.15}$ and $PSCFN_{0.2}$ exhibit higher resistances of 0.063 Ω·cm^2 and 0.071 Ω cm^2, the undoped PSCF sample demonstrates the highest polarization resistance at 0.188 Ω cm^2. As summarized in Table S4, the $PSCFN_{0.05}$ and $PSCFN_{0.1}$ exhibit relatively low polarization resistance at 800°C compared to many conventional SOFC cathodes, such as $La_{0.6}Ca_{0.4}Fe_{0.8}Co_{0.2}O_{3-\delta}$ (LCFC, 0.062 Ω cm^2). These results highlight the competitive advantage of Nb-doped PSCF in achieving superior electrochemical performance for SOFC applications. This trend can be attributed to the dual role of Nb in modifying the cathode properties. At low to moderate doping levels (≤ 10%), Nb^{5+} incorporation increases the oxygen vacancy concentration by introducing charge imbalance and slightly distorts the perovskite lattice, both of which promote oxygen ion diffusion and surface exchange. In contrast, excessive Nb doping introduces several negative effects as follows: (1) The site-blocking effect, where electrochemically inactive Nb^{5+} replaces Co/Fe cations at the B-site, reduces the number of active sites for oxygen adsorption and electron transfer, and (2) the over-stabilization of lattice oxygen, as Nb^{5+} forms stronger Nb–O bonds, suppressing oxygen vacancy formation and mobility, which hinders both bulk oxygen ion transport and surface exchange. These explanations are consistent with the Arrhenius plots in Figure 4F, where $PSCFN_{0.1}$ shows the lowest activation energy (1.30 eV), whereas both $PSCFN_{0.15}$ and $PSCFN_{0.2}$ exhibit increased activation energies of 1.33 and 1.37 eV, respectively. To further investigate the impedance behavior, DRT

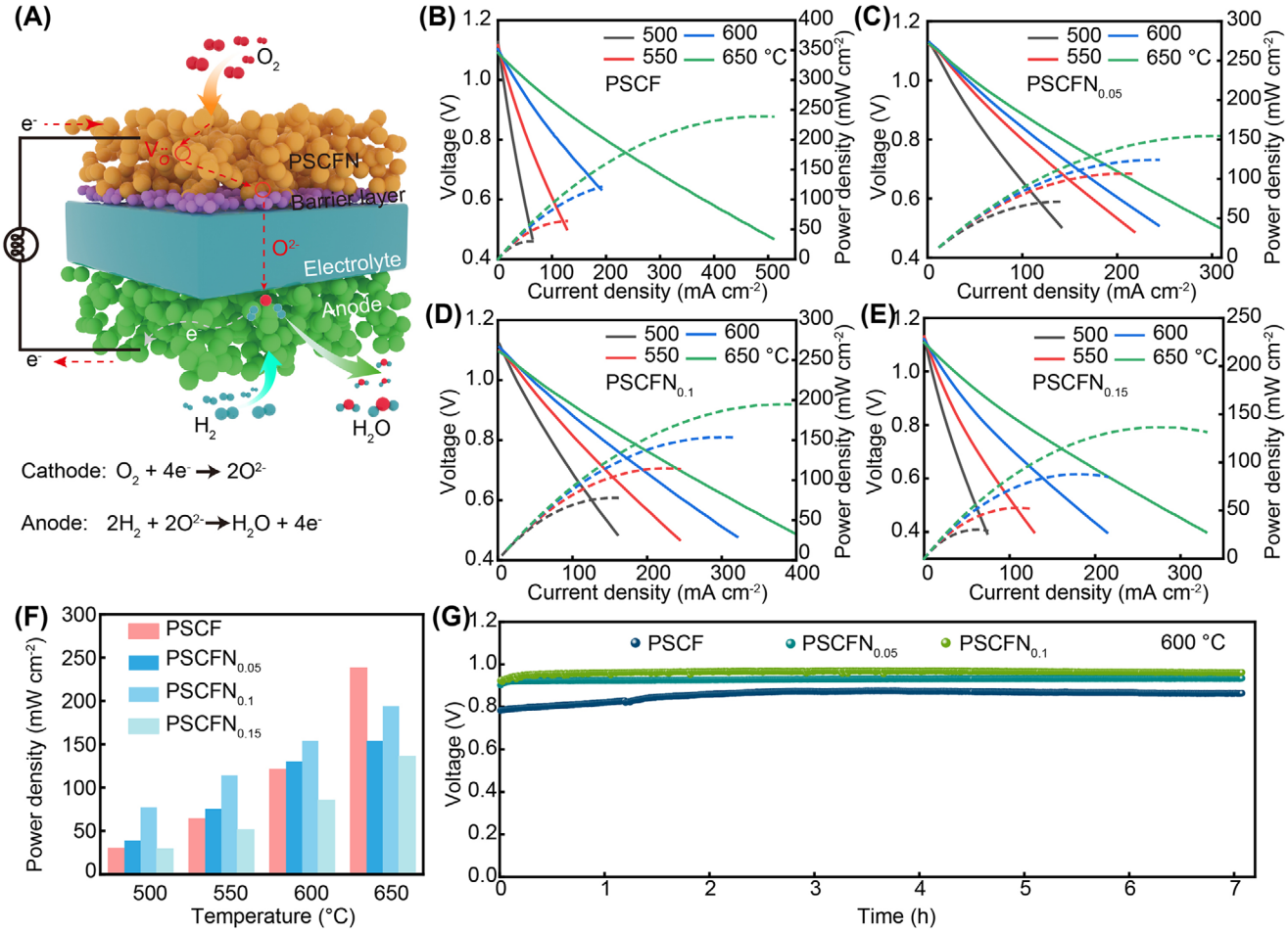

FIGURE 5 | Single-cell performance of Nb-doped PSCF cathodes. (A) Schematic of the single-cell configuration. Single-cell performance at different temperatures for various Nb doping levels: (B) PSCF, (C) $PSCF_{0.05}$, (D)$PSCFN_{0.1}$, and (E) $PSCFN_{0.15}$. (F) Statistical distribution of the output power densities for each cell. (G) Short-term stability test curve of PSCF, $PSCFN_{0.05}$, and $PSCFN_{0.1}$ cathodes at 600°C.

analysis was performed. At 800°C (Figure 4G), the undoped PSCF exhibits four distinct peaks: one in the mid-frequency range (~10–10^2 Hz) indicating limitations in oxygen surface exchange, and another in the high-frequency region (~10^3 Hz) associated with charge transfer. Additionally, two low-frequency peaks (< 10 Hz) reflect challenges in oxygen ion diffusion [7, 13, 23, 46]. Upon moderate Nb doping ($PSCF_{0.05}$ and $PSCFN_{0.1}$), all peaks become less pronounced, indicating a general acceleration of the ORR kinetics. In particular, $PSCFN_{0.1}$ displays the most compressed DRT profile, with significantly diminished mid- and low-frequency peaks, suggesting more efficient surface exchange and oxygen ion transport. However, further Nb incorporation ($PSCFN_{0.15}$ and $PSCFN_{0.2}$) results in the reappearance and intensification of the mid- and low-frequency peaks. This indicates a deceleration of both surface exchange and diffusion steps, in line with the increasing R_p and activation energy values. These results reinforce the conclusion that excessive Nb doping impairs ORR activity by limiting oxygen vacancy mobility and reducing the number of catalytically active B-site cations. Figure 4H presents the DRT analysis of $PSCFN_{0.1}$ at different temperatures, showing that at 500°C, the high impedance is primarily due to slower oxygen diffusion. With increasing temperature, the impedance associated with each relaxation process decreases, suggesting that higher temperatures promote oxygen adsorption, diffusion, and charge transfer. However, at 700°C and 800°C, charge transfer remains the dominant factor influencing ORR kinetics, as evidenced by a prominent peak in the high-frequency region. To further evaluate the CO_2 tolerance of the perovskite oxide, EIS measurements were performed in sequential environments of air, 5% CO_2, and 10% CO_2 at 600°C (Figure S11A). Both PSCF and $PSCFN_{0.1}$ showed an increase in polarization resistance in CO_2-containing atmospheres, due to the decreased oxygen partial pressure, which hinders oxygen surface exchange. Upon returning to air, the resistance values recovered, indicating no irreversible degradation. Fourier transform infrared (FTIR) spectra were also collected after exposing the cathode pellets to pure CO_2 for 10 h at 600°C (Figure S11B). Characteristic carbonate absorption peaks were observed at 1060, 1248, and 1391 cm^{-1}. Compared to PSCF, the intensity of these peaks was significantly reduced in $PSCFN_{0.05}$ and $PSCFN_{0.1}$, suggesting that moderate Nb doping suppresses carbonate formation, enhancing CO_2 tolerance. However, at higher doping levels (0.15 and 0.2), the intensity of the peaks increased, indicating that excessive Nb doping compromises carbonate suppression and CO_2 stability. Therefore, moderate Nb doping provides the best CO_2 tolerance.

A preliminary evaluation of Nb-doped PSCF cathodes was conducted using single-cell configurations. As shown in Figure 5A

and Figure S12A, oxygen molecules reduction at the cathode to form oxygen ions, which are transported through the GDC barrier and electrolyte layers to the anode for reaction with hydrogen, facilitating energy conversion. Figure S12B shows the porous microstructure of the cathode. However, due to the substantial thickness of the anode support (~400 μm) and cathode layer (~100 μm), notable overall resistance was observed below 500°C, limiting low-temperature performance. Based on physicochemical characterizations combined with DFT calculations, moderate Nb substitution was found to modulate the Co^{4+}/Fe^{4+}-related active sites, promoting improved ORR kinetics in the intermediate-temperature. Consequently, performance evaluations were carried out from 500°C to 650°C. As presented in Figure 5B–F, single cells employing $PSCFN_{0.05}$ and $PSCFN_{0.1}$ cathodes consistently outperformed both undoped and over-doped samples at 500–600°C. For instance, at 500°C, the power density of $PSCFN_{0.1}$ reached 77 $mW{\cdot}cm^{-2}$, over 2.6 times higher than that of PSCF (29 $mW{\cdot}cm^{-2}$). A similar trend was observed at 550°C and 600°C, where $PSCFN_{0.1}$ delivered peak outputs of 114 and 154 $mW{\cdot}cm^{-2}$, respectively, clearly surpassing PSCF and $PSCFN_{0.15}$. And at elevated temperatures above 650°C, the performance advantage of $PSCFN_{0.1}$ becomes less pronounced. As shown in Figure S13, the undoped PSCF cathode eventually outperforms its doped counterparts, likely due to the dominant contribution of Co^{3+}/Fe^{3+}-related redox activity at high temperatures, where Nb doping may impede electronic conductivity or disrupt the optimal balance of oxygen vacancies at high temperature. The EIS results for the full cells, shown in Figure S14, further support these findings. As temperature increased from 500°C to 800°C, all samples exhibited decreased total impedance, indicating thermally activated electrochemical processes. Notably, at 500–600°C, $PSCFN_{0.05}$ and $PSCFN_{0.1}$ displayed smaller arc radii compared to undoped PSCF, reflecting their lower polarization resistance and improved ORR activity. However, at higher temperatures (650–800°C), this trend diminished, and $PSCFN_{0.1}$ even exhibited higher impedance than PSCF at 800°C, suggesting that the positive effect of Nb doping is less pronounced under high-temperature conditions. Short-term stability tests at 600°C (Figure 5G) further confirmed the advantage of moderate Nb doping. $PSCFN_{0.05}$ and $PSCFN_{0.1}$ maintained stable output voltages throughout the 7-h test without noticeable decay, indicating excellent durability for the measured duration. In contrast, the undoped PSCF cell required nearly 2 h to stabilize. These results highlight that moderate Nb doping optimally tunes the electronic and ionic characteristics for efficient performance at 500–600°C.

3 | Conclusion

In conclusion, this study investigates the impact of Nb^{5+} substitution at the B-site of PSCF on the structural. DFT calculations reveal that Nb doping leads to a redistribution of oxygen vacancies, significantly reducing the vacancy formation energy around Co/Fe sites while increasing it at Nb-related sites. This site-selective modulation facilitates oxygen ion migration in the lattice and enhances surface oxygen exchange dynamics. Experimental characterizations—including O_2-TPD, XPS, and DRT analyses—further confirm improved surface oxygen activity and accelerated rate-limiting steps of the ORR at moderate doping levels. Notably, doping with 5–10 mol% Nb effectively reduces the polarization resistance (0.050 $\Omega{\cdot}cm^2$ at 800°C for $PSCFN_{0.1}$) and enhances power output by more than 2.6 times at 500°C compared to undoped PSCF. However, excessive Nb incorporation (≥ 15 mol%) leads to over-stabilization of oxygen vacancies and a decline in active site availability, ultimately impeding ORR kinetics and diminishing cathodic performance. These findings underscore the dual role of Nb doping it enhances oxygen defect chemistry and ORR kinetics at optimized levels yet introduces performance limitations when over-doped. This work demonstrates that rational control of high-valence dopants is essential to balance vacancy generation, charge transport, and catalytic activity, offering strategic guidance for the design of advanced perovskite cathodes for intermediate-temperature SOFCs.

4 | Experimental Section

4.1 | Preparation of Nb-Doped Perovskite Oxide Cathodes

According to previous reports, the perovskite oxide powder is synthesized using the sol-gel method [13, 47]. Stoichiometric amounts of $Pr(NO_3)_3{\cdot}6H_2O$, $Co(NO_3)_2{\cdot}6H_2O$, $Sr(NO_3)_2$, $Fe(NO_3)_3{\cdot}9H_2O$, and $Nb(HC_2O_4)_5$ (niobium oxalate) were used as the metal ions precursor. The molar ratios of the metal precursors were adjusted to achieve the desired stoichiometry of $Pr_{0.4}Sr_{0.6}Co_{0.2}Fe_{0.8-x}Nb_xO_{3-\delta}$, where x corresponds to the Nb content (0, 0.05, 0.1, 0.15, and 0.2), producing the compositions $PSCFN_{0.05}$, $PSCFN_{0.1}$, $PSCFN_{0.15}$, and $PSCFN_{0.2}$, respectively.

To promote homogeneous mixing and stable chelation of the metal ions, the chemicals were dissolved in deionized water, and citric acid and ethylenediaminetetraacetic acid (EDTA) were added as complexing agents. The molar ratios of citric acid to total metal ions and EDTA to total metal ions were maintained at 1.5:1 and 1:1, respectively. Ammonia solution was slowly added to adjust the pH of the solution to approximately 8, enhancing the stability of the metal complexes. The precursor solution was concentrated via rotary evaporated at 45°C until a viscous brown gel was formed. This gel was then dried in a tube furnace under flowing argon at 250°C for 30 min to remove excess organics. After cooling to room temperature, the resulting dried precursor was sintered in air at 1000°C for 5 h to ensure complete decomposition of organics and formation of the perovskite oxide phase. During calcination, one end of the tube furnace was connected to a narrow air inlet tube flanged to the furnace (instead of being fully open to ambient air), while the other end was connected to a vacuum-assisted exhaust system equipped with a scrubber to safely remove gaseous byproducts. Finally, the calcined product was manually ground to obtain the perovskite oxide powders.

4.2 | Fabrication of Cells

In the fabrication process, a 5% polyvinyl butyral (PVB) ethanol solution was used as a binder, and commercially sourced GDC powder (provided by SOFCMAN, Ningbo, China) was pressed at 8 MPa for 20 min to produce a 10 mm diameter and 600 μm thickness GDC electrolyte pellet, serving as the support layer for the symmetric cell. An anode-supported substrate from SOFC was employed as the base for the single-cell, with a

structural configuration consisting of a 400 μm NiO-YSZ anode layer, a 10 μm YSZ electrolyte layer, and a 2 μm GDC barrier layer. The synthesized perovskite oxides were utilized as cathode materials, with ethyl cellulose as a binder and soluble starch as a pore-forming agent. The cathode slurry was applied onto the electrolyte and the anode substrate through screen-printing, forming the symmetric cell and single-cell structures.

4.3 | Characterizations and Measurements

The XRD (Bruker D8 Discover) with Cu-Kα was employed to determine the crystal structure and analyze the change of lattice parameters. Field-emission SEM (JEOL 7600) was used to observe detailed microstructural features, particle morphology, and distribution, with EDS employed for elemental analysis. TEM (JEOL JEM-1400) was conducted to further observe detailed nanostructures of the cathode powders. XPS (Physical Electronics Inc. Quantera II) was used to examine the surface chemical composition and valence states of ions present. Thermal analyzer (STA449 F3, NETZSCH, Germany) was used for thermogravimetric testing of the cathode powders under vacuum atmosphere. Prior to the measurement, powder samples were pretreated at 100°C under vacuum for 8 h to remove most of the surface-adsorbed oxygen. The oxygen nonstoichiometry (δ) was estimated based on the mass loss associated with oxygen release during heating. The calculation followed the equation:

$$\delta \propto \frac{M_{O_2} \cdot \Delta m_{O_2}}{W}$$

where Δm_{O_2} is the mass loss attributed to oxygen release, M_{O_2} is the molar mass of oxygen, and W the total sample mass. This method provides a quantitative estimation of the oxygen vacancy concentration in the synthesized perovskite oxides. Oxygen adsorption and desorption behaviors were analyzed by O_2-TPD (BSD-Chem C200). The samples were pretreated by heating from room temperature to 200°C at a rate of 10°C/min in a helium (He) flow of 50 sccm for 1 h. After cooling to 50°C, a 25 sccm flow of 20% O_2/He was introduced for 1 h to achieve saturation. Subsequently, the flow was switched back to 50 sccm of helium for 1 h to remove weakly adsorbed surface oxygen. Desorption was then conducted in a He atmosphere by increasing the temperature to 1000°C at a rate of 10°C/min, with the desorbed gases monitored via a thermal conductivity detector (TCD). The thermal expansion behavior was measured using a thermomechanical analyzer (TMA; NETZSCH TMA 402F3, Germany) in the range of 30–900°C. FTIR spectroscopy (PerkinElmer Frontier) was used to identify carbonate formation and assess the CO_2 tolerance of the cathode materials. The EIS were obtained using a Metrohm Autolab electrochemical workstation (PGSTAT302N) across a frequency range of 0.1 Hz to 1 MHz with an amplitude of 10 mV and used the software provided by Metrohm Autolab to fit it. The I-V characteristics of the fuel cell were measured using a SOFC test setup from Fiaxell SOFC Technologies. During the tests, the single-cell was placed in a KITTEC Squadro muffle furnace, with the cell sandwiched between the anode and cathode collector discs. The setup was connected to gas-tight fittings for the delivery of air (flow rate: 300 sccm) and hydrogen (flow rate: 150 sccm) to the cell. The tests were conducted at temperatures ranging from 500°C to 600°C, and the I-V characteristics were obtained using slow-scan galvanostatic linear sweep voltammetry (LSV).

4.4 | DFT Calculations

First-principles calculations were conducted to explore the influence of Nb doping on electrochemical performance, employing the VASP with projector augmented wave (PAW) pseudopotentials [12, 43]. The generalized gradient approximation (GGA) with Perdew–Burke–Ernzerhof (PBE) parameterization was used to treat the exchange-correlation functional. $Pr_{0.5}Sr_{0.5}Co_{0.25}Fe_{0.75}O_{3-\delta}$ was selected as the model compound to improve computational efficiency. A $2 \times 2 \times 2$ supercell was constructed for bulk calculations, while surface modeling utilized a stable (001) orientation, represented by a four-layer slab with 15 Å of vacuum and eight ABO_3 unit cells. For oxygen adsorption energy calculations, the lower two slab layers remained fixed, while the upper layers were fully relaxed. BO_2-terminated surfaces were used exclusively, given prior findings of enhanced ORR activity at B-site elements [48]. The first Brillouin zone integration applied a $5 \times 5 \times 5$ k-point mesh for bulk and a $5 \times 5 \times 1$ mesh for slab models, with a plane-wave cutoff of 500 eV. Self-consistent field (SCF) convergence was achieved when the total energy change was less than 10^{-8} eV. Structural optimizations used the conjugate gradient (CG) method, with ion relaxation convergence set at 10^{-3} eV/Å to ensure precise structural adjustment during energy minimization.

The oxygen vacancy formation energy (E_{vac}) is calculated using the following equation:

$$E_{vac} = E_{def} + \frac{1}{2}E_{O_2} - E_{per} \quad (3)$$

where E_{def} and E_{per} represent the total electronic energies of the defective and perfect PSCF or PSCFN surfaces (or bulk structures), respectively. The oxygen adsorption energy (E_{ads}) on the PSCF and PSCFN surfaces is calculated using the equation:

$$E_{ads} = E_{slab+O_2} - E_{slab} - E_{O_2} \quad (4)$$

E_{slab}, E_{slab+O_2}, and E_{O_2} represent the total energies of the clean surface, the surface with adsorbed oxygen, and the isolated oxygen molecules, respectively.

Projected density of states (PDOS) was calculated based on the relaxed bulk structures using a $5 \times 5 \times 5$ k-point mesh and the tetrahedron method with Blöchl corrections, with the Fermi level set to 0 eV.

Acknowledgments

This work was supported by A*STAR-MAECI Joint Grant Call–Scientific and Technological Cooperation Grant, Award No. R23I0IR039 and in part by the Italian Ministry of Foreign Affairs and International Cooperation, Grant Number SG23GR06.

Conflicts of Interest

The authors declare no conflicts of interest.

References

1. Y. Wang, J. Shi, X. Gu, O. Deutschmann, Y. Shi, and N. Cai, "Toward Mobility of Solid Oxide Fuel Cells," *Progress in Energy and Combustion Science* 102 (2024): 101141.

2. H. Helal, M. Ahrouch, A. Rabehi, D. Zappa, and E. J. C. Comini, "Nanostructured Materials for Enhanced Performance of Solid Oxide Fuel Cells: A Comprehensive Review," *Crystals* 14, no. 4 (2024): 306.

3. G. Yang, C. Su, H. Shi, et al., "Toward Reducing the Operation Temperature of Solid Oxide Fuel Cells: Our Past 15 Years of Efforts in Cathode Development," *Energy & Fuels* 34, no. 12 (2020): 15169–15194.

4. J. Zhang, S. Ricote, P. V. Hendriksen, and Y. Chen, "Advanced Materials for Thin-Film Solid Oxide Fuel Cells: Recent Progress and Challenges in Boosting the Device Performance at Low Temperatures," *Advanced Functional Materials* 32, no. 22 (2022): 2111205.

5. S. Pirou, B. Talic, K. Brodersen, et al., "Production of a Monolithic Fuel Cell Stack With High Power Density," *Nature Communications* 13, no. 1 (2022): 1263.

6. Z. Shao and S. M. Haile, "A High-Performance Cathode for the Next Generation of Solid-Oxide Fuel Cells," *Nature* 431, no. 7005 (2004): 170–173.

7. P. Zhang, J. Chang, F. Qu, et al., "Clean and Sustainable Power to X to Power by Reversible Symmetrical Solid Oxide Cells With Highly Active Ferrite Perovskite Electrodes," *ACS Sustainable Chemistry & Engineering* 12, no. 4 (2024): 1561–1572.

8. A. Weber, "Fuel Flexibility of Solid Oxide Fuel Cells," *Fuel Cells* 21, no. 5 (2021): 440–452.

9. T. Hibino, A. Hashimoto, T. Inoue, J.-I. Tokuno, S.-I. Yoshida, and M. Sano, "A Low-Operating-Temperature Solid Oxide Fuel Cell in Hydrocarbon-Air Mixtures," *Science* 288, no. 5473 (2000): 2031–2033.

10. M. Li, M. Zhao, F. Li, et al., "A Niobium and Tantalum Co-Doped Perovskite Cathode for Solid Oxide Fuel Cells Operating Below 500 °C," *Nature Communications* 8, no. 1 (2017): 13990.

11. P. Kaur and K. Singh, "Review of Perovskite-Structure Related Cathode Materials for Solid Oxide Fuel Cells," *Ceramics International* 46, no. 5 (2020): 5521–5535.

12. H. Li, M. Wei, Y. Liu, et al., "Enhanced Mechanisms of Oxygen Reduction on $Pr_{0.4}Sr_{0.6}Co_{0.2}Fe_{0.8}O_{3-\delta}$ Impregnated $La_{1-x}Sr_xCo_{1-y}Fe_yO_{3-\delta}$ Cathodes for Solid Oxide Fuel Cells," *Journal of Alloys and Compounds* 927 (2022): 167033.

13. X. Yu, Z. Wang, R. Ren, et al., "In Situ Self-Reconstructed Nanoheterostructure Catalysts for Promoting Oxygen Reduction Reaction," *ACS Energy Letters* 7, no. 9 (2022): 2961–2969.

14. M. Yashima, T. Tsujiguchi, Y. Sakuda, et al., "High Oxide-Ion Conductivity Through the Interstitial Oxygen Site in $Ba_7Nb_4MoO_{20}$-Based Hexagonal Perovskite Related Oxides," *Nature Communications* 12, no. 1 (2021): 556.

15. K. T. Lee, A. A. Lidie, H. S. Yoon, and E. D. Wachsman, "Rational Design of Lower-Temperature Solid Oxide Fuel Cell Cathodes via Nanotailoring of Co-Assembled Composite Structures," *Angewandte Chemie International Edition* 53, no. 49 (2014): 13463–13467.

16. C. Yao, H. Zhang, X. Liu, J. Meng, J. Meng, and F. Meng, "A Niobium and Tungsten Co-Doped $SrFeO_{3-\delta}$ Perovskite as Cathode for Intermediate Temperature Solid Oxide Fuel Cells," *Ceramics International* 45, no. 6 (2019): 7351–7358.

17. J. Y. Koo, H. Kwon, M. Ahn, et al., "Suppression of Cation Segregation in $(La,Sr)CoO_{3-\delta}$ by Elastic Energy Minimization," *ACS Applied Materials & Interfaces* 10, no. 9 (2018): 8057–8065.

18. S. O. Gil, L. M. Toscani, S. A. Larrondo, and D. G. Lamas, "Synthesis of $Sr_2(Co_{1.1};Mo_{0.9})O_{6-\delta}$ Double Perovskite and Its Electrochemical Performance in the Oxygen Reduction Reaction," *Ceramics International* 50, no. 24 (2024): 53867–53876.

19. F. Chen, D. Zhou, X. Xiong, et al., "Doping Strategy on Improving the Overall Cathodic Performance of Double Perovskite $LnBaCo_2O_{5+\delta}$ (Ln=Pr, Gd) as Potential SOFC Cathode Materials," *Journal of Materiomics* 9, no. 5 (2023): 825–837.

20. Y. Wang, Y. Wang, H. Qi, et al., "Tuning the ORR Catalytic Activity of $LaFeO_{3-\delta}$-Based Perovskite Cathode for Solid Oxide Fuel Cells by Doping With Alkaline-Earth Metal Elements," *Ceramics International* 50, no. 3 (2024): 5818–5826.

21. N. Ai, S. P. Jiang, Z. Lü, K. Chen, and W. Su, "Nanostructured $(Ba,Sr)(Co,Fe)O_{3-\delta}$ Impregnated $(La,Sr)MnO_3$Cathode for Intermediate-Temperature Solid Oxide Fuel Cells," *Journal of the Electrochemical Society* 157, no. 7 (2010): B1033.

22. Y. Yin, H. Dai, S. Yu, L. Bi, and E. Traversa, "Tailoring Cobalt-Free $La_{0.5}Sr_{0.5}FeO_{3-\delta}$ Cathode With a Nonmetal Cation-Doping Strategy for High-Performance Proton-Conducting Solid Oxide Fuel Cells," *SusMat* 2, no. 5 (2022): 607–616.

23. Y. Hou, L. Wang, L. Bian, Q. Zhang, L. Chen, and K.-C. Chou, "Effect of High-Valence Elements Doping at B Site of $La_{0.5}Sr_{0.5}FeO_{3-\delta}$," *Ceramics International* 48, no. 3 (2022): 4223–4229.

24. S. Vázquez, L. Suescun, and R. Faccio, "Effect of Cu Doping on $Ba_{0.5}Sr_{0.5}Fe_{1-x}Cu_xO_{3-\delta}$ Perovskites for Solid Oxide Fuel Cells: A First-Principles Study," *Journal of Power Sources* 311 (2016): 13–20.

25. C. Yang, Z. Yang, C. Jin, G. Xiao, F. Chen, and M. Han, "Sulfur-Tolerant Redox-Reversible Anode Material for Direct Hydrocarbon Solid Oxide Fuel Cells," *Advanced Materials* 24, no. 11 (2012): 1439–1443.

26. S. Sengodan, S. Choi, A. Jun, et al., "Layered Oxygen-Deficient Double Perovskite as an Efficient and Stable Anode for Direct Hydrocarbon Solid Oxide Fuel Cells," *Nature Materials* 14, no. 2 (2015): 205–209.

27. Y. Guo, D. Chen, H. Shi, R. Ran, and Z. Shao, "Effect of Sm^{3+} Content on the Properties and Electrochemical Performance of $Sm_xSr_{1-x}CoO_{3-\delta}$ ($0.2 \leq x \leq 0.8$) as an Oxygen Reduction Electrodes on Doped Ceria Electrolytes," *Electrochimica Acta* 56, no. 7 (2011): 2870–2876.

28. J. Zhang, X. Li, Z. Zhang, et al., "A New Highly Active and CO_2-Stable Perovskite-Type Cathode Material for Solid Oxide Fuel Cells Developed From A- and B-Site Cation Synergy," *Journal of Power Sources* 457 (2020): 227995.

29. B. S. Teketel, B. A. Beshiwork, X. Luo, et al., "A-Site Doping Enabled Higher-Oxygen-Vacancy Cobalt-Free Layered Perovskite Cathode for Higher-Performing Protonic Ceramic Fuel Cells," *Ceramics International* 48, no. 24 (2022): 37232–37241.

30. Y. Ren, R. Küngas, R. J. Gorte, and C. Deng, "The Effect of A-Site Cation (Ln = La, Pr, Sm) on the Crystal Structure, Conductivity and Oxygen Reduction Properties of Sr-Doped Ferrite Perovskites," *Solid State Ionics* 212 (2012): 47–54.

31. F. Zhou, L. Zhou, M. Hu, et al., "Pd-Doped $La_{0.6}Sr_{0.4}Co_{0.2}Fe_{0.8}O_{3-\delta}$ Perovskite Oxides as Cathodes for Intermediate Temperature Solid Oxide Fuel Cells," *Solid State Ionics* 319 (2018): 22–27.

32. X. Lu, Y. Yang, Y. Ding, et al., "Mo-Doped $Pr_{0.6}Sr_{0.4}Fe_{0.8}Ni_{0.2}O_{3-\delta}$ as Potential Electrodes for Intermediate-Temperature Symmetrical Solid Oxide Fuel Cells," *Electrochimica Acta* 227 (2017): 33–40.

33. Q. Zhou, L. Zhang, and T. He, "Cobalt-Free Cathode Material $SrFe_{0.9}Nb_{0.1}O_{3-\delta}$ for Intermediate-Temperature Solid Oxide Fuel Cells," *Electrochemistry Communications* 12, no. 2 (2010): 285–287.

34. C. Geng, M. Li, X. Fang, et al., "Enhanced Electrocatalytic Activity of $SrFe_{0.9}Nb_{0.1}O_{3-\delta}$ Through In-Situ Synthesis of $Sr_3Fe_{1.8}Nb_{0.2}O_{7-\delta}$ Coating," *Ceramics International* 50, no. 18 (2024): 31752–31758.

35. K. Partovi, B. Geppert, F. Liang, C. H. Rüscher, and J. Caro, "Effect of the B-Site Composition on the Oxygen Permeability and the CO_2 Stability of $Pr_{0.6}Sr_{0.4}Co_xFe_{1-x}O_{3-\delta}$ ($0.0 \leq x \leq 1.0$) Membranes," *Chemistry of Materials* 27, no. 8 (2015): 2911–2919.

36. H. Hayashi, T. Saitou, N. Maruyama, H. Inaba, K. Kawamura, and M. Mori, "Thermal Expansion Coefficient of Yttria Stabilized zirconia for Various Yttria Contents," *Solid State Ionics* 176, no. 5 (2005): 613–619.

37. J.-H. Lee, K. N. Kim, J.-W. S. J. Kim, B.-K. Kim, H.-W. Lee, and J. Moon, "An Investigation of the Interfacial Stability Between the Anode and Electrolyte Layer of LSGM-Based SOFCs," *Journal of Materials Science* 42 (2007): 1866–1871.

38. G. Zhang, Z. Liu, N. Zhu, W. Jiang, X. Dong, and W. Jin, "A Novel Nb_2O_5-Doped $SrCo_{0.8}Fe_{0.2}O_{3-\delta}$ Oxide With High Permeability and Stability for Oxygen Separation," *Journal of Membrane Science* 405–406 (2012): 300–309.

39. Y. Qiu, H. Li, Y. Liu, B. Chi, J. Pu, and J. Li, "Effects of Niobium Doping on the Stability of $SrCo_{0.2}Fe_{0.8}O_{3-\delta}$ Cathodes for Intermediate Temperature Solid Oxide Fuel Cells," *Journal of Alloys and Compounds* 829 (2020): 154503.

40. Y. Wang, D. Zhou, W. Zhang, et al., "CoO_X Composite $Pr_{0.4}Sr_{0.6}Co_{0.2}Fe_{0.8}O_{3-\delta}$ Perovskite Was Used to Obtain an IT-SOFC Cathode With High Electrocatalytic Activity," *Fuel* 381 (2025): 133422.

41. Y. Li, X. Chen, Y. Yang, Y. Jiang, and C. Xia, "Mixed-Conductor $Sr_2Fe_{1.5}Mo_{0.5}O_{6-\delta}$ as Robust Fuel Electrode for Pure CO_2 Reduction in Solid Oxide Electrolysis Cell," *ACS Sustainable Chemistry & Engineering* 5, no. 12 (2017): 11403–11412.

42. G. C. Kostogloudis, P. Fertis, and C. Ftikos, "The Perovskite Oxide System $Pr_{1-x}Sr_xCo_{1-y}Mn_yO_{3-\delta}$: Crystal Structure and Thermal Expansion," *Journal of the European Ceramic Society* 18, no. 14 (1998): 2209–2215.

43. M. Wei, H. Li, S. Wu, et al., "First-Principles Study of Oxygen Reduction Reaction on Pd-Doped $La_xSr_{1-x}Co_yFe_{1-y}O_{3-\delta}$ Cathodes of Solid Oxide Fuel Cells," *International Journal of Hydrogen Energy* 44, no. 54 (2019): 28720–28730.

44. M. Pavone, A. M. Ritzmann, and E. A. Carter, "Quantum-Mechanics-Based Design Principles for Solid Oxide Fuel Cell Cathode Materials," *Energy & Environmental Science* 4, no. 12 (2011): 4933.

45. J. K. Nørskov, T. Bligaard, J. Rossmeisl, and C. H. Christensen, "Towards the Computational Design of Solid Catalysts," *Nature Chemistry* 1, no. 1 (2009): 37–46.

46. D. A. Osinkin, "An Approach to the Analysis of the Impedance Spectra of Solid Oxide Fuel Cell Using the DRT Technique," *Electrochimica Acta* 372 (2021): 137858.

47. W. Yang, T. Hong, S. Li, et al., "Perovskite Sr_{1-x} Ce_x $CoO_{3-\delta}$ ($0.05 \leq x \leq 0.15$) as Superior Cathodes for Intermediate Temperature Solid Oxide Fuel Cells," *ACS Applied Materials & Interfaces* 5, no. 3 (2013): 1143–1148.

48. Y. A. Mastrikov, S. Guo, F. Puleo, L. F. Liotta, and E. A. Kotomin, "First Principles Modeling of Pd-Doped (La,Sr)(Co,Fe)O_3 Complex Perovskites," *Fuel Cells* 16, no. 2 (2016): 267–271.

Supporting Information

Additional supporting information can be found online in the Supporting Information section.

Supplementary File: sus270037-sup-0001-SuppMat.docx.